MINIREVIEW

Check for updates

Flexible two-dimensional MXene-based antennas

Xingce Fan, [ID] †[ab] Xiaohu Zhang,†[ab] Ya Li,[d] Hongjun He,[d] Qixing Wang,[d] Leilei Lan, [ID] [ae] Wenzhe Song,[ab] Teng Qiu [ID] *[ab] and Weibing Lu*[bc]

With the growing development of the Internet of things, wearable electronic devices have been extensively applied in civilian and military fields. As an essential component of data transmission in wearable electronics, a flexible antenna is one of the key aspects of research. Conventional metal antennas suffer from a large skin depth, and cannot satisfy the requirements of wearable electronics such as light weight, flexibility, and thinness. Recently, a group of two-dimensional metallic metal carbides (named MXenes) have been explored as building blocks for high-performance flexible antennas with excellent flexibility and superior mechanical strength. The appearance of hydrophilic functional groups at the surface of a MXene allows simple, scalable, and environmentally friendly manufacturing of MXene-based antennas. In this minireview, some pioneering works of MXene-based flexible radio frequency components are summarized, and the existing bottlenecks and the future trends of this promising field are discussed.

[a] School of Physics, Southeast University, Nanjing 211189, China.
  E-mail: tqiu@seu.edu.cn
[b] Center for Flexible RF Technology, Frontiers Science Center for Mobile Information
  Communication and Security, Southeast University, Nanjing 210096, China
[c] State Key Lab of Millimeter Waves, School of Information Science and Engineering,
  Southeast University, Nanjing 210096, China. E-mail: wblu@seu.edu.cn
[d] Future Research Laboratory, China Mobile Research Institute, Beijing, China
[e] School of Mechanics and Optoelectronic Physics, Anhui University of Science and
  Technology, Huainan 232001, China
† X. Fan and X. Zhang contributed equally.

1. Introduction

With the growing development of the Internet of things, wearable electronic devices have been extensively used in civilian and military fields,[1,2] such as human motion detection,[3] medical aids,[4] and electronic skins.[5–7] As an essential component of wearable electronic devices, a flexible antenna is the focus of research because it serves as a medium for signal transmission and directly affects the performance of the entire system. Common antennas are made of copper with high electrical conductivity.[8,9] However, the performance of thin and flexible metal antennas is restricted by an intrinsic property called the skin depth, which is frequency-dependent. The principle of skin

Dr Xingce Fan is currently a postdoc at the School of Physics at Southeast University (SEU, China). He received his BS degree in Applied Physics and PhD in Physics from SEU in 2014 and 2020, respectively. From 2017 to 2019, he was affiliated with Prof. Oliver G. Schmidt's research group at the Leibniz Institute for Solid State and Materials Research (IFW Dresden, Germany). His research interests include the synthesis of plasmonic and semiconductor nanomaterials and their applications in nanophotonics.

Xingce Fan

Xiaohu Zhang is currently a master student at the School of Physics at Southeast University (SEU, China). He received his BS degree in Applied Physics from SEU in 2020. His research interests include the synthesis of two-dimensional MXene materials and their applications in wearable electronics.

Xiaohu Zhang

depth effect requires the antennas thickness to be at least several micrometers to ensure a sufficient space for the currents to flow.[10] It is extremely challenging to balance the flexibility and conductivity of antennas, thereby making it urgent to find new alternative conductive materials for flexible wearable electronic devices.

In the past decade, conductive two-dimensional (2D) materials, such as graphene[11,12] and some metallic transition metal dichalcogenides,[13] have been explored for the manufacturing of flexible radio frequency (RF) wireless communication devices. Replacement of metals with 2D materials will result in antennas with flexible, high-transmittance, and light weight features, which have been predicted to be the mainstream materials for next-generation flexible RF devices.[14] For example, graphene nanosheets were successfully printed on a flexible substrate with high resolution to achieve a flexible wideband dipole antenna.[15] Later on, a printable radio frequency identification antenna by low temperature processing of graphene ink was also demonstrated, which shows a conductivity of 4.3×10^4 S m^{-1} with a thickness of 6 μm.[16] The metallic 2D NbSe$_2$ thin film, featuring a conductivity of 9.7×10^5 S m^{-1} with a sub-micrometer thickness of 0.85 μm, has also been demonstrated to be a high-performance sub-micrometer RF antenna.[13] Although the behavior of waves propagating through 2D materials at the RF regime has not yet been fully explained theoretically, the experimental evidence shows that all these nanomaterials perform at thicknesses below their predicted skin depth, enabling 2D materials as rising stars in the construction of high-performance flexible RF communication devices. At present, the biggest obstacle in the wide applications of 2D materials in RF communication devices is their insufficient conductivities, which always need incorporation of conductive additives to achieve a reasonable RF performance.

Since 2011, a new class of two-dimensional transition metal carbides,[17] carbonitrides,[18] and nitrides[19] have been discovered as promising materials for their excellent performance in supercapacitors,[20–22] sodium-ion capacitors,[23] lithium-ion batteries,[24,25] catalysis,[26] chemical sensing,[27–30] biomedical devices,[31] and flexible electronics.[32–35] They are named MXenes and have a general formula of $M_{n+1}X_nT_x$ (n = 1, 2, and 3), where M is a transition metal, X is carbon and/or nitrogen, and T$_x$ denotes terminal groups (–OH, –O, and –F). They are typically synthesized by a top-down approach by selectively etching the ''A'' layer from their precursor MAX phases. Some MXenes exhibit high electrical conductivity (over 10^6 S m^{-1}), excellent flexibility, and superior mechanical strength.[36] Owing to the appearance of hydrophilic functional groups at the surface of a MXene, simple, scalable, and environmentally friendly manufacturing of MXene films from aqueous solutions with no surfactant or binder is possible.[37] Some pioneering works show the potential of MXenes for flexible RF communication devices, paving the way for wide applications of 2D MXenes in flexible wearable electronics.[38–41] This minireview intends to summarize the recent cutting-edge works of 2D MXene-based flexible antennas, discuss the existing bottlenecks, and give some guidelines for the future development of this promising field.

2. Synthesis of MXene nanoflakes and film patterning techniques

2.1. Synthesis of MXene nanoflakes

In comparison with other 2D materials held together by van der Waals force, the bonds in MAX are too strong to be broken by shear or any similar mechanical method. 2D MXenes $M_{n+1}X_nT_x$ (n = 1, 2, and 3) are produced by etching out the A layers from the parent MAX phases (as shown in Fig. 1a and b).[18,42] The M–A bonds show much higher strength than the M–X bonds, making it possible to selectively etch the A layer by a chemical approach without disrupting the M–X bonds.[43] The etching approaches of MAX in a HF aqueous solution[17,18] or in a mixture of strong acids and fluoride salts[44] are extensively employed to synthesize MXenes at room temperature. The removal of A atoms

Teng Qiu

Prof. Teng Qiu is currently a full-time professor at the School of Physics at Southeast University (SEU, China). He received his BS degree in Chemistry and PhD in Condensed Matter Physics from Nanjing University (NJU, China) in 2002 and 2007, respectively. From 2004 to 2008, he was affiliated with Prof. Paul K. Chu's research group in City University of Hong Kong (CityU, China). In 2010, he held an Alexander von Humboldt fellow position in the Leibniz Institute for Solid State and Materials Research Dresden (IFW Dresden, Germany). His current research interests include surface science and engineering of two-dimensional materials and their applications in nanophotonics.

Weibing Lu

Prof. Weibing Lu received his PhD degree in Microwave Technology from SEU in 2005 and has been working in the State Key Laboratory of Millimeter Waves of SEU since the same year. Now he is the director of the Research Center of Flexible RF Technology and the president of the Research Institute of Southeast University. His main research interests include flexible RF technology, electromagnetic compatibility, and applied computational electromagnetics.
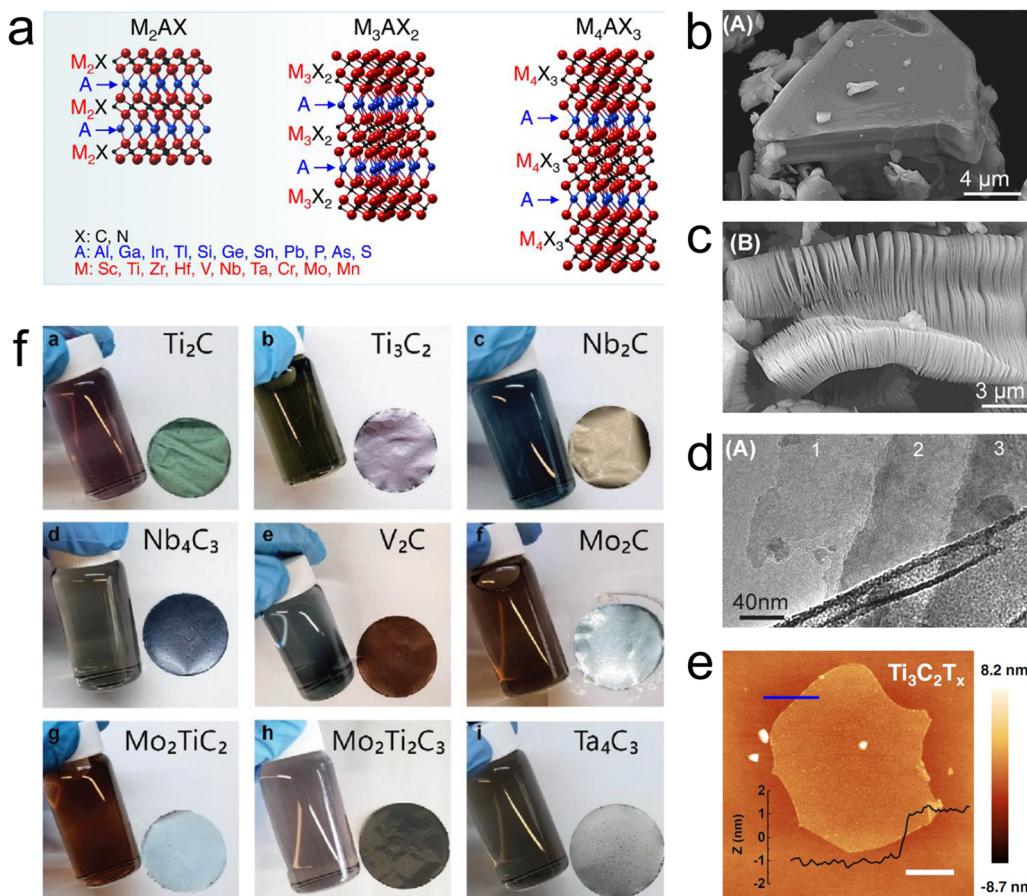
Fig. 1 Synthesis of MXene nanoflakes. (a) Schematics of the MAX phase: M_2AX, M_3AX_2, and M_4AX_3. Scanning electron microscopy (SEM) images of (b) bulk Ti_3AlC_2 crystals, (c) HF-etched multilayered Ti_3C_2 MXene, (d) HF-etched and delaminated few-layered and monolayered Ti_3C_2 MXenes, and (e) atomic force microscopy (AFM) image of few-layered Ti_3C_2 MXene. (f) Digital photographs of MXene colloidal dispersions and the corresponding free-standing films fabricated by vacuum-assisted filtration. Copyrights: (a) Reprinted with permission from ref. 42. Copyright 2017 Macmillan Publishers Limited, part of Springer Nature. (b–d) Reprinted with permission from ref. 18. Copyright 2012 American Chemistry Society. (e) Reprinted from ref. 48. (f) Reprinted with permission from ref. 49. Copyright 2020 Wiley-VCH GmbH.

from the MAX phase dramatically weakens the interaction between the $M_{n+1}X_nT_x$, thus resulting in a multilayered feature (as shown in Fig. 1c). The etching process can be well controlled by adjusting the etchant concentration, etching time, and temperature to produce complete conversion of MAX into MXenes.[42] After the intercalation and delamination, the multilayered MXenes could be further exfoliated into few-layered and even monolayered MXenes (Fig. 1d).[18] The intercalation of multilayered MXenes could be achieved by adding some small polar organic molecules, such as hydrazine, urea, dimethyl sulfoxide,[45] and isopropylamine,[46] as well as some large molecules, such as tetrabutylammonium hydroxide (TBAOH),[30] choline hydroxide or n-butylamine.[47] The delaminated MXenes show an atomic thin feature with lateral size reaching tens of micrometers (Fig. 1e).[48] Because of the arching of hydrophilic groups on the outside of MXenes, the delaminated few-layered or monolayered MXenes show stable colloidal suspensions for a long time, which can be further engineered to produce MXene membranes with flexible, robust and conductive features (Fig. 1f).[49] The detailed synthesis of various MXene materials has been well reviewed in several papers, which could supply more comprehensive view of the promising MXene family.[25,27,36,50–54]

2.2. Fabrication and patterning of MXene films

Advanced patterning techniques continuously stimulate the scalable and mass-produced flexible devices. The MXene nanoflakes can be dispersed in an aqueous solution due to their abundant surface terminal functional groups, thus enabling the readily processing of MXene films by vacuum-assisted filtration, spin coating, blade-coating, electrophoretic deposition, rolling compression, spray coating, and printing methods. For instance, Lukatskaya et al. demonstrated a vacuum-assisted filtration method by filtrating the $Ti_3C_2T_x$ colloidal solution through nano-porous polypropylene membranes to achieve a planar "paper" electrode architecture for horizontally aligned MXene nanoflakes (Fig. 2a).[55] The MXene films can be peeled off after drying, presenting a freestanding feature. The MXene films are of densely compacted layers with the electrode density approaching 4 g cm^{-3}. Other similar approaches to prepare MXene films have also been developed. Spin-coating of MXene
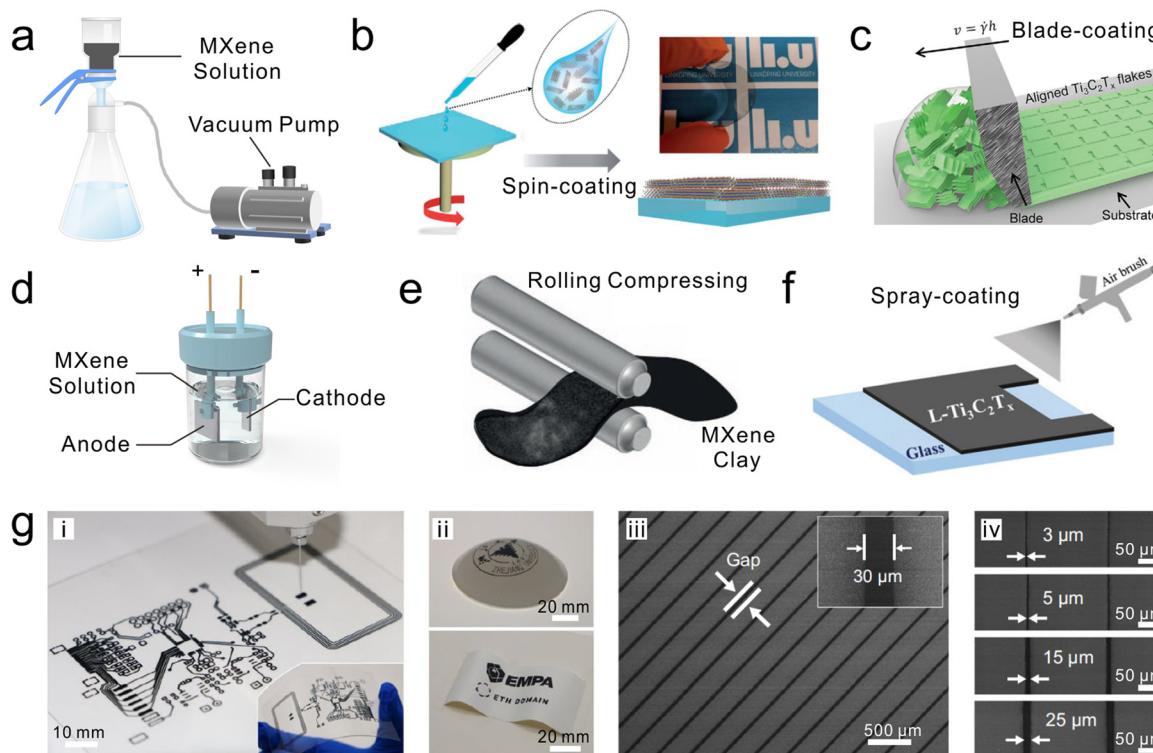
Fig. 2 Fabrication and patterning of MXene films. Schematics of (a) vacuum-assisted filtration, (b) spin-coating, (c) blade-coating, (d) electrophoretic deposition, (e) rolling compression, (f) spray-coating of MXene films. (g) (i) Optical image of high-resolution integrated MXene circuits fabricated by the printing technique; (ii) MXene printed ''ZJU'' and ''EMPA'' logos on curved surfaces; (iii) SEM image of the printed periodically MXene lines with a gap of 30 μm; (iv) SEM images of MXene lines with different gaps from 3 μm to 25 μm. Copyrights: (b) Reprinted with permission from ref. 56. Copyright 2020 The Royal Society of Chemistry. (c) Reprinted with permission from ref. 57. Copyright 2020 WILEY-VCH Verlag GmbH & Co. KGaA, Weinheim. (e) Reprinted with permission from ref. 44. Copyright 2014 Macmillan Publishers Limited. (f) Reprinted with permission from ref. 59. Copyright 2016 The Royal Society of Chemistry. (g) Reprinted from ref. 41.

is one of the most convenient techniques to prepare smooth MXene films. Qin et al. fabricated an MXene-based all-solution processed transparent flexible electrode by spin-coating a layer of small-sized $Ti_3C_2T_x$ nanoflakes on the substrates (Fig. 2b).[56] Their results verified that the $Ti_3C_2T_x$ MXene nanoflakes tend to result in a horizontally aligned configuration under the effect of the shear force, which could maintain the robustness of flexible MXene films during bending or twisting in practical applications. Zhang et al. demonstrate a high-performance free-standing MXene film with both improved strength and electrical conductivity using a blade-coating method without the use of any binders or additives (Fig. 2c).[57] They produced several meters of a continuous, 940 nm-thick MXene film that exhibited the highest tensile strength (568 ± 24 MPa) and Young's modulus (20.6 ± 3.1 GPa). After vacuum drying, the blade-coated MXene films reach an electrical conductivity value of $\sim 1.51 \times 10^6$ S m^{-1}. As shown in Fig. 2d, Collini et al. investigated the electrophoretic depositions of MXene films with a thickness of 3 to 10 μm, which shows the highest conductivity of $\sim 7.4 \times 10^5$ S m^{-1}.[58] Ghidiu et al. reported a method of producing MXenes using a solution of lithium fluoride and hydrochloric acid. The resulting hydrophilic MXenes can be rolled into flexible and free-standing films with a thickness of tens of micrometers and a conductivity of

$\sim 1.5 \times 10^5$ S m^{-1} (Fig. 2e).[44] Peng et al. also demonstrated a spray-coating method to prepare all-MXene interdigital micro-supercapacitors, in which the $Ti_3C_2T_x$ MXene aqueous solution was sprayed on the substrate by using a commercial airbrush, which is followed by treatment with a hot air gun to dry the coated MXene films simultaneously (Fig. 2f). The interdigital structures were patterned using a photoresist-free direct laser cutting method, which enables the fabrication of desired patterns. However, its spatial resolution of patterning is insufficient for the fabrication of some flexible devices which needs higher processing precision.[59]

In 2022, Shao et al. reported a room-temperature direct printing strategy with a high printing resolution for flexible wireless electronics (as schematically shown in Fig. 2g(i)).[41] Additive-free $Ti_3C_2T_x$ MXene aqueous ink was prepared by a minimally modified intensive layer delamination approach, where the optimized centrifugation and ultrasonic methods were adopted to improve the rheological and electrical properties. Because of the high ink concentration (~ 60 mg mL^{-1}), ultrathin thickness (~ 1.5 nm), large monolayer ratio ($>90\%$), and narrow lateral size distribution (~ 1.6 μm), the as-prepared $Ti_3C_2T_x$ MXene aqueous ink shows desirable shear-thinning viscoelastic properties (viscosity of $\sim 2.5 \times 10^2$ Pa s), allowing continuous extrusion and quick ink solidification. The synthesized $Ti_3C_2T_x$

MXene aqueous ink is stable for at least two years when stored in Ar-sealed bottles in dark and low temperature (<4 °C) environments. Furthermore, they demonstrated the room temperature direct printing technique on a programmable three-axis pneumatic extrusion dispenser. The MXene line width and gap dimension can be predefined, and the patterns can be efficiently printed on a planar or curved surface on demand (Fig. 2g(ii)). As shown in Fig. 2g(iii) and (iv), the ordered MXene lines with the precise gap of 30 μm and the MXene lines with precise line gaps ranging from 3 to 30 μm could be readily printed, demonstrating the high printing precision of this method. The printed MXene lines are composed of densely stacked and interconnected $Ti_3C_2T_x$ nanosheets, allowing the fast transport of free electrons. The electrical conductivity of the printed MXene line was estimated to $\sim 6.3 \times 10^5$ S m^{-1} and can be further optimized to $\sim 6.9 \times 10^5$ S m^{-1} by storing under low-humidity conditions. The high precision printing and superior electrical conductivity are extremely beneficial to the scalable fabrication of flexible RF devices, especially the flexible patch transmission lines as well as other RF wireless communication devices.

At present, vacuum-assisted filtration, spray-coating, and printing method have been successfully applied to the fabrication of flexible MXene-based antennas, which hold the promise of scalable and massive production in future. They are suitable for the patterning of additive-free MXene solutions. Other methods, such as spin-coating, blade-coating, electrophoretic deposition, and rolling compressing, have been demonstrated effective to fabricate MXene-based energy devices but have not yet been demonstrated for the preparation of flexible MXene-based antennas. Generally, the etched additive-free MXene without further delamination presents a multilayered feature, which always brings about cracks during bending or twisting, resulting in the decline of conductivity. However, these methods may be efficient in processing the hybrid of MXene and other materials (such as carbon nanotubes and Ag wires).

3. MXene-based flexible radio frequency components

3.1. MXene-based flexible transmission lines (TLs)

Transmission lines (TLs) are the basic element in RF devices, and typically transmit electromagnetic fields containing information from one point to another point along the path defined by TLs. Especially, TLs generally serve as feeding lines in flexible devices, whose performance determines the efficiency of flexible antennas. A low loss transmission is always required for highly efficient signal delivery. The propagation of an electromagnetic field along the MXene TLs was investigated by Sarycheva et al.[38] As shown in Fig. 3a, an MXene-based coplanar waveguide (CPW) consisting of a central conductor and two side conductors was fabricated. The MXene-based antenna with the thickness exceeding 1.4 μm was fabricated by vacuum-assisted filtration and that with the thickness lower
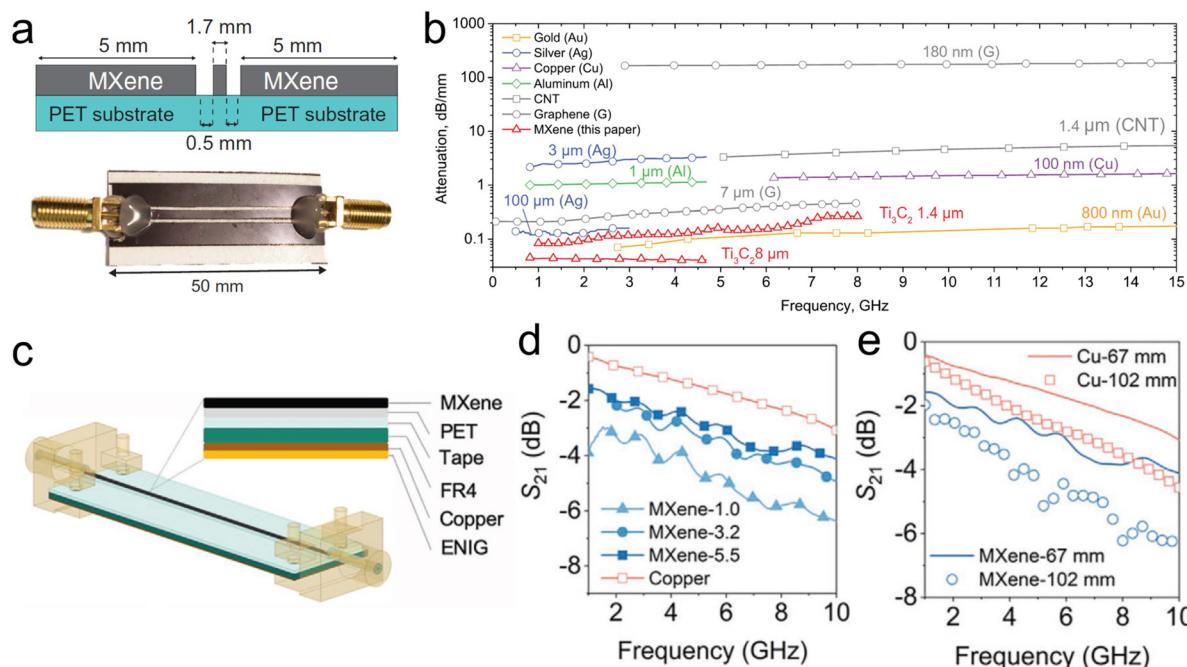
Fig. 3 MXene-based transmission lines (TLs). (a) Schematic and digital photos of the 1.4 μm-thick MXene CPW TLs. (b) Comparison of attenuation in CPW of different materials: graphene, carbon nanotubes (CNTs), silver ink, silver-polydimethylsiloxane, gold ink, aluminum, copper, and 1.4 and 8 μm-thick Ti_3C_2 MXene TLs. (c) Schematic of the configuration of MXene microstrip TLs; the inset of the cross-sectional view showing the materials of different layers. (d) Transmission coefficient S_{21} of 67 mm-long MXene TLs with different thicknesses; a 67 mm-long copper TL with a thickness of 35 μm was used as a reference. (e) The transmission coefficient S_{21} of MXene TLs with different lengths (67 and 102 mm); 35 μm-thick copper TLs with the same dimensions were measured as a reference. Copyrights: (a and b) Reprinted from ref. 38 under the terms of the CC BY-NC license, Copyright 2018 The Authors. (c–e) Reprinted with permission from ref. 39. Copyright 2020 Wiley-VCH GmbH.

than 1.4 μm was fabricated by spray-coating. The reflection (S_{11}) and transmission (S_{21}) coefficients were monitored to evaluate the performance of MXene TLs. They demonstrated that the attenuation increases with the decrease of the thicknesses of MXene TLs, indicating that the relatively thicker MXene TLs are beneficial to the transmission of an electromagnetic field. Fig. 3b presents the attenuations of different antenna materials, where the 1.4 μm-thick Ti_3C_2 MXene TL shows much lower loss than the other material TLs from 1 to 8 GHz, and the 8 μm-thick Ti_3C_2 MXene TL shows the lowest loss, indicating Ti_3C_2 MXene to be a great candidate for manufacturing ultrathin RF devices.

Later on, Han *et al.* demonstrated Ti_3C_2 MXene-based microstrip TLs, which were fabricated by spray-coating the Ti_3C_2 MXene solution onto the pre-patterned flexible substrates (as shown in Fig. 3c).[39] The transmission coefficient S_{21} of MXene microstrip TLs with different thicknesses was evaluated as shown in Fig. 3d. The increased transmission loss of all TLs with the frequency from 1 to 10 GHz is primarily caused by skin depth effects. The transmission loss decreases with the increase of MXene thickness, which is attributed to the decreased MXene sheet resistance. Especially, the results show that the transmission loss of a 5.5 μm-thick MXene TL approaches that of a 35 μm-thick copper TL. As shown in Fig. 3e, they also demonstrated that the longer MXene and Cu TLs show higher transmission loss with the increase of frequency from 1 to 10 GHz. The transmission loss of the 102 mm-long MXene TL approaches the that of the 67 mm-long copper TL, indicating that MXene has the potential to replace copper in the future fabrication of flexible devices.

3.2. MXene-based flexible antennas

3.2.1. MXene-based flexible radio frequency identification (RFID) antennas.
The radio frequency identification (RFID) technique uses the wireless radio frequency approach to conduct the non-contact bidirectional data exchange. RFID can read and write the recorded media in an electronic label or a radio frequency card to achieve the purpose of target identification and the data exchange. RFID is extensively utilized in typical applications such as inventory control, equipment tracking, personnel tracking, and mobile payment. A typical RFID system is comprised of two components: RFID tags and RFID readers. The RFID tags could be passive or active to deliver their identity and other information to the nearby readers.

In 2018, Sarycheva *et al.* developed MXene-based RFID tags by spray-coating, which have slightly different loop sizes, thus enabling the matching conditions at different frequencies.[38] A general mechanism of the RFID working principle is shown in Fig. 4a, where a signal is sent from an RFID reader and received by an RFID tag connected to an RFID chip. Using the chip, the signal is transformed and backscattered to the RFID reader, thus performing the reading and writing of information. The downlink reading distances of the three different MXene-based RFID tags are shown in Fig. 4b, which enable a reading range above 6 m at peak frequency and almost 8 m when maximum matching is achieved. In 2022, Shao *et al.* printed an MXene-based RFID sensing system as shown in Fig. 4c.[41] The printed MXene-based RFID tags exhibit a wide frequency band with a peak near the typical working frequency of 920 MHz. Afterwards, they applied the MXene-based RFID tags on a temperature monitoring system, which is based on the backscatter coupling between the RFID reader and tag. As shown in Fig. 4d, they demonstrated the detection of local temperature on the human body, exhibiting high consistency and sensitivity upon temperature variations.

Apart from the far field identification, near-field communication (NFC) is another type of RFID technology, which enables simultaneous power and data transmission between
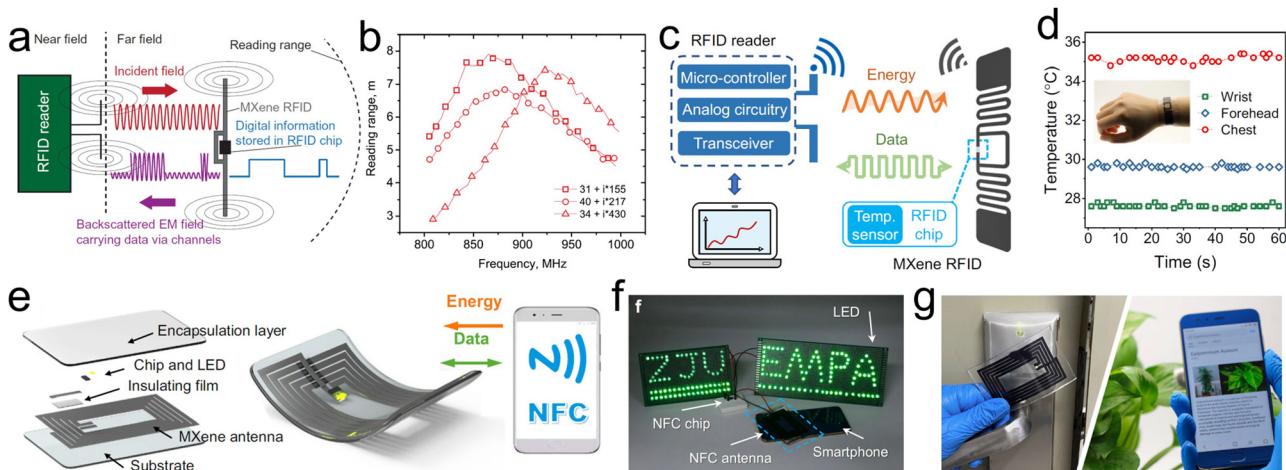

Fig. 4 MXene-based radio frequency identification antennas. (a) The schematics of working principles of RFID. (b) The performance of MXene-based RFID with various characteristic impedances. Reprinted from ref. 38 under the terms of the CC BY-NC license, Copyright 2018 The Authors. (c) Schematic mechanism of the MXene-based RFID temperature tag with a laptop-connected RFID reader. (d) MXene RFID temperature tags as wearable sensors to monitor the surface temperature on the human body. (e) Fabrication and working mechanisms of MXene-based NFC tags which communicate wirelessly with the nearby smartphones or electronic devices. (f) The electrical energy transmitted to MXene-based NFC antennas from an NFC-enabled smartphone. (g) Two examples of application of MXene-based NFC tags, access cards for standard electronic door locks (left) and identification labels for plant information (right). Reprinted from ref. 41.

devices through inductive coupling. Shao *et al.* printed the first MXene-based NFC antenna of 70 mm length and 45 mm width, referencing the standard size of credit cards (shown in Fig. 4f).[41] The MXene-based NFC antennas show stable accessibility at 13.56 MHz for various NFC-enabled equipment. As shown in Fig. 4g, they demonstrated that NFC antennas could harvest energy from a cellphone and exchange information with nearby devices, such as access cards for standard electronic door locks and plant identification labels.

3.2.2. MXene-based flexible dipole antennas. A half-wave dipole antenna is one of the most common antennas used for radio and telecommunications. A half-wave dipole antenna consists of two conductive elements like wires, rods, or bands, where the total length of conductive elements is about half of the working wavelength. A half-wave dipole antenna shows an isotropic pattern and radiates an electromagnetic field with a donut-shaped pattern. In 2018, Sarycheva *et al.* reported the first MXene-based half-wave dipole antenna (as shown in Fig. 5a).[38] The Ti_3C_2 MXene-based dipole antenna was designed to work at 2.4 GHz, which is widely used for Wi-Fi and bluetooth applications. As shown in Fig. 5b, the total length of the MXene-based dipole antennas is ∼62 mm, which are fabricated by a spray-coating technique. The performance of dipole antennas was evaluated by the return loss and radiation properties. As shown in Fig. 5c, the MXene-based dipole antennas with different thicknesses from 114 nm to 8 μm were fabricated and the return losses were evaluated to be from −12 to −65 dB, respectively. The 8 μm-thick MXene dipole antenna shows a reflection coefficient of ∼−65 dB, which is sufficient to deliver energy to the free space. The radiation efficiency was also measured to confirm that the transmitted energy could be radiated into free space rather than dissipated by Ohmic loss. Fig. 5d shows the radiation pattern of an 8 μm-thick MXene-based dipole antenna with the maximum radiation in the perpendicular direction and the nulls in the longitudinal direction. The maximum gain was acquired on a 1.4 μm-thick dipole antenna with the value of 2.11 dB. Although the predicted skin depth of MXene at a frequency of 2.4 GHz is ∼10 μm, the MXene-based antenna with the thickness lower than 1 μm was still able to radiate effectively and provide good matching to the reference impedance.

Li *et al.* designed a crumple-textured flexible dipole antenna composed of MXene nanosheets and single-walled carbon nanotubes (S-MXene) on the latex.[40] The crumple-textured S-MXene films were fabricated by transferring a layer of the filtered S-MXene membrane onto a pre-strained latex substrate. Fig. 5e shows the optical image of S-MXene dipole antennas, which consist of two symmetric pieces of stretchable S-MXene conductors separated by an insulating gap. During the stretching process of the S-MXene dipole antenna, the return losses were measured as shown in Fig. 5f, where the return loss of all the antennas was all below −30 dB under 0%, 50%, 100%, and 150% uniaxial strains, demonstrating the reflected power less than 0.1% at all stretching states. The crumple-textured morphologies were gradually deformed into periodic wrinkles with the increase of uniaxial strains (as shown in Fig. 5g). Meanwhile, the resonant frequencies of S-MXene dipole antennas linearly decreased from 1.575 to 1.375 GHz as the uniaxial strains increased from 0% to 150%, which can be attributed to the variation in antenna length during the stretching. They also demonstrated that the S-MXene dipole antenna showed nearly the same return loss (−33 dB) at the same resonant frequency
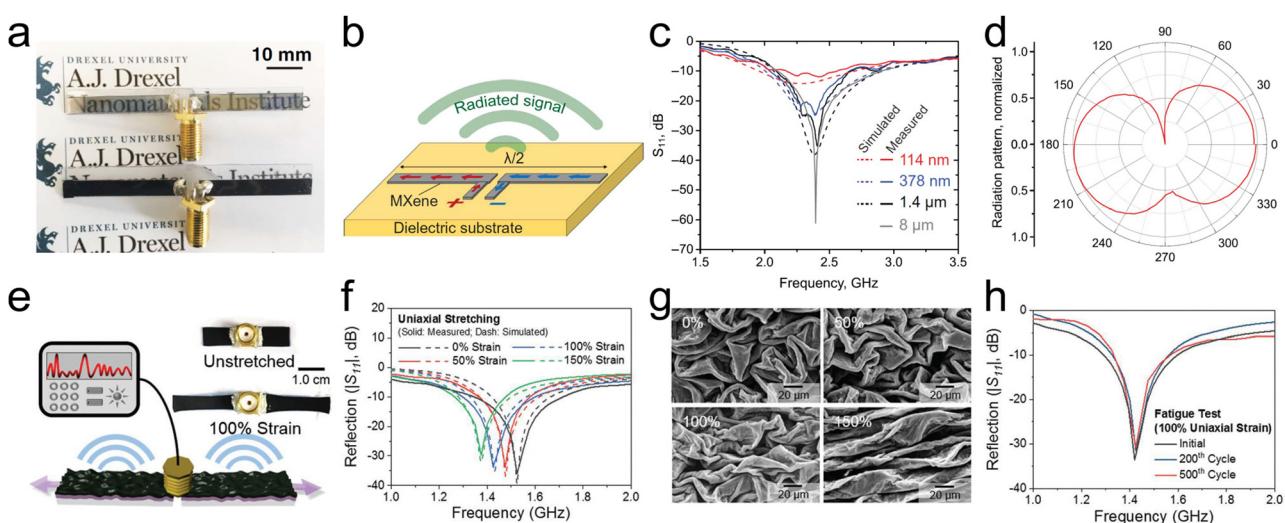

Fig. 5 MXene-based dipole antennas. (a) Digital photos showing 62 nm-thick (top) and 1.4 μm-thick (bottom) MXene-based dipole antennas. (b) Schematic explaining the working principle of the dipole antenna. The length of the dipole antenna matches half of the wavelength of the radiated signal. (c) S_{11} parameter (reflection coefficient) of dipole antennas of different thicknesses (114 nm, 378 nm, 1.4 μm, and 8 μm). (d) Typical radiation pattern of the 8 μm-thick MXene antenna measured in the anechoic chamber. Reprinted from ref. 38 under the terms of the CC BY-NC license, Copyright 2018 The Authors. (e) Schematic illustration and digital photos (right) of an S-MXene dipole antenna at different stretching states. (f) Measured and simulated reflection $|S_{11}|$ and resonant frequencies of an S-MXene antenna under different uniaxial strains. (g) SEM images of S-MXene coatings of antenna wings under different uniaxial strains. (h) Performance of stretchable S-MXene antennas during 200- and 500-cycles fatigue tests with the uniaxial strain of up to 100%. Reprinted with permission from ref. 40. Copyright 2019 WILEY-VCH Verlag GmbH & Co. KGaA, Weinheim.
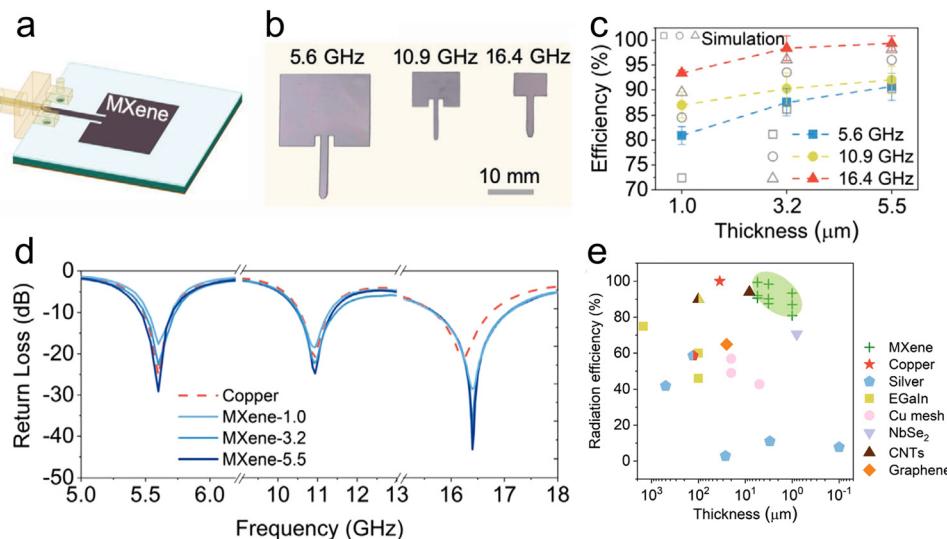
Fig. 6 MXene-based microstrip patch antennas. (a) Schematic of a $Ti_3C_2T_x$ MXene-based microstrip patch antenna on the dielectric substrate with an SMA connector. (b) Digital image of MXene-based microstrip patch antennas at the three target frequencies of 5.6, 10.9, and 16.4 GHz. (c) Return loss of MXene-based microstrip patch antennas with different thicknesses of 1.0, 3.2, and 5.5 μm at different target frequencies; copper-based patch antennas with the same geometry and dimensions were used as references. (d) Measured and simulated radiation efficiency of MXene-based microstrip patch antennas of different thicknesses at different frequencies. (e) A comparison of radiation efficiency *versus* thickness of MXene with metals, carbons, and others as patch antennas. Reprinted with permission from ref. 39. Copyright 2020 Wiley-VCH GmbH.

(1.425 GHz) during the fatigue test up to 100% uniaxial strains for 500 cycles (as shown in Fig. 5h).

3.2.3. MXene-based flexible microstrip patch antennas. Flexible antennas with higher frequencies used in RF, particularly fifth-generation (5G) communications, are in significant demand due to the explosive growth of portable and wearable electronics in the 5G network. In 2020, Han *et al.* first demonstrated MXene-based flexible microstrip patch antennas (Fig. 6a).[39] The $Ti_3C_2T_x$ MXene nanosheets aqueous solution was spray-coated on the polyethylene terephthalate (PET) substrates. The flexible patch antennas with target frequencies of 5.6, 10.9, and 16.4 GHz were readily obtained by predefining the PET substrate shape (Fig. 6b). They demonstrated the performance of flexible patch antennas in terms of return loss

and radiation properties. As shown in Fig. 6c, all the three flexible patch antennas with different thicknesses have a return loss of less than −15 dB. The radiation efficiencies of 5.5 μm-thick MXene-based patch antennas were measured to be 90% at 5.6 GHz, 92% at 10.9 GHz, and 99% at 16.4 GHz, which show almost the same performance when compared with those of copper antennas (Fig. 6d). But the MXene-based patch antennas show only 15% of the thickness and 7% of the weight of copper antennas. The comparison of radiation efficiencies with other material antennas is shown in Fig. 6e, indicating that the MXene-based patch antennas show a copper-comparable radiation performance but with much thinner and lighter features. They also designed an MXene-based antenna system based on MXene TLs and MXene patch antennas for 5G

Table 1 Summary of the flexible MXene-based RF components

Type	Material	Fabrication method	Conductivity (S m⁻²)	Thickness (μm)	Return loss (dB)	Gain	Radiation efficiency	Frequency	Ref.
RFID	Ti_3C_2 MXene	Spray coating	8.0×10^5	1	N/A	N/A	N/A	860–925 MHz	38
RFID	Ti_3C_2 MXene	Printing	6.9×10^5	12	N/A	N/A	N/A	920 MHz	41
NFC	Ti_3C_2 MXene	Printing	6.9×10^5	12	N/A	N/A	N/A	13.56 MHz	41
Dipole	Ti_3C_2 MXene	Spray coating	8.0×10^5	8.0	−65	2.0 dB	N/A	2.4 GHz	38
				1.4	−36	1.7 dB			
				0.548	−39	−1.5 dB			
Dipole	Ti_3C_2-carbon nanotube/Latex	Vacuum-assisted ?thyc?> filtration	2.9×10^5	N/A	−30 to −36	N/A	N/A	1.375–1.575 GHz	40
Dipole	Ti_3C_2 MXene	Vacuum-assisted ?thyc?> filtration	2.5×10^5	0.286	−12.2	N/A	N/A	1.24 GHz	61
Patch	Ti_3C_2 MXene	Spray coating	1.51×10^6	1.0	−17 to −30	5.0 ∼ 5.5 dBi	80.0–93.4%	5.6, 10.9 and 16.4 GHz	39
				3.2	−23 to −40	5.0 ∼ 5.5 dBi	87.0–98.4%		
				5.5	−29 to −48	5.48 ∼ 7.14 dBi	90.6–99.0%		
Patch array	Ti_3C_2 MXene	Spray coating	1.51×10^6	5.5	−40	11 dBi	83.0%	28.0 GHz	39
Patch	Ti_3C_2 MXene	Vacuum-assisted filtration	N/A	3	−38.9	2 dB	N/A	1.834 GHz	62

communications. The MXene antenna system is composed of flexible patch arrays (1 × 4) on a conformal substrate, which are connected by an MXene TL feeding network and separated linearly by a distance of half wavelength. The integrated MXene antenna arrays can operate at a target frequency in practical 5G communication of 28 GHz with the radiation efficiency exceeding 83%. Other flexible MXene patch antennas have also been investigated. Khorsand Kazemi et al. demonstrated lightweight MXene-based circular patch antennas, which were made by vacuum-assisted filtration.[60] The designed circular antenna shows an operation frequency of 1.841 GHz and an amplitude of −38.895 dB and features 57% of the thickness and 26.66% of the weight in comparison with the copper-based antenna with similar configurations (Table 1).

4. Summary and perspectives

The development of MXene nanoscience has catalyzed the advancement of MXene-based RF components because of their superior conductivity. In this minireview, the synthesis of MXene nanoflakes and the patterning method of flexible MXene-based RF components are discussed. The state-of-the-art research progress of MXene-based flexible RF components, such as RF TLs, RFID tags, RF dipole and microstrip patch antennas, is also summarized. However, there is still a long way to go to improve the performance of MXene antennas and broaden their application fields.

(1) At present, MXene flakes are mostly synthesized using HF or molten salts etching approaches, which are efficient but environmentally unfriendly. Efficient, scalable, cost-efficient, and environmentally friendly etching techniques should be further explored for acquiring high-quality MXene materials.

(2) MXenes are always unstable, which are easily oxidized after etching. The surface chemistry may provide passivation, but it is necessary to guarantee their conductivity simultaneously. The high-performance RF devices require a low Ohmic loss to guarantee better transmission of signals. How to further improve the conductivity of MXene materials still remains a challenge.

(3) MXene-based antennas made of multilayered MXene powder cannot satisfy the flexibility because cracks are always created during bending or twisting, and the conductivity is generally severely affected at this time. Therefore, it is worth paying more attention to the delamination technique for acquiring few-layered or monolayered MXenes, which enables the MXene-based flexible devices to have a more robust configuration and a higher conductivity. The incorporation with other conductive materials is also an approach to promote the efficiency of flexible antennas.

(4) Flexible antennas are essential components in wearable electronics, which require antennas of advanced features, such as easy to wear and conformity to the human body, deformability, and light weight. Advanced patterning techniques of flexible antennas on various substrates should be further developed.

(5) Several pioneering works have demonstrated that the MXene-based antenna can function well even below the predicted skin depth. Sarycheva et al. demonstrated that the signal attenuation increases as the thickness of MXenes decreases from 8 μm to 62 nm. The attenuation of MXene films with a thickness of 1.4 μm is approaching that with a thickness of 8 μm. Besides, although the skin depth of Ti_3C_2 was estimated to be ∼10 μm at 2.4 GHz, MXene-based antennas with their thickness approaching 1 μm were still confirmed to show good performance.[38] However, the underlying mechanism should be studied for a better understanding of the wave transmission behavior along the MXene films, which is significant for the trade-off between flexibility and conductivity.

(6) MXene-based RF TLs always show a large energy loss at a higher frequency, which require the tightly bounded fields to minimize undesired radiation and coupling. Additionally, MXene-based flexible antennas working at higher frequency (over 10 GHz) with high radiation efficiency are favorable for a variety of applications ranging from wearable electronics to the Internet of things (IoT) devices and satellite communications.

(7) Since MXene-based microstrip antennas are often integrated with other microwave circuitry, a balance between good antenna performance and circuit design must be achieved. Moreover, it is of potential interest to produce MXene-based antenna arrays for acquiring higher gain and greater directivities.

Author contributions

X. Fan and X. Zhang wrote the manuscript. T. Qiu and W. Lu. revised the manuscript. Y. Li, H. He, Q. Wang, L. Lan and W. Song gave some useful suggestions. All authors have given approval to the final version of the manuscript. X. Fan and X. Zhang contributed equally.

Conflicts of interest

The authors declare no conflicts of interest.

Acknowledgements

References

1 H. C. Ates, P. Q. Nguyen, L. Gonzalez-Macia, E. Morales-Narváez, F. Güder, J. J. Collins and C. Dincer, *Nat. Rev. Mater.*, 2022, **7**, 887–907.

2 R. De Fazio, M. De Vittorio and P. Visconti, *Electronics*, 2021, **10**, 1660.

3 X. G. Yu, Y. Q. Li, W. B. Zhu, P. Huang, T. T. Wang, N. Hu and S. Y. Fu, *Nanoscale*, 2017, **9**, 6680–6685.

4 C. A. Tavera, J. H. Ortiz, O. I. Khalaf, D. F. Saavedra and T. H. H. Aldhyani, *Comput. Math. Methods Med.*, 2021, **2021**, e5574376.

5 L. Wang, K. Jiang and G. Shen, *Adv. Mater. Technol.*, 2021, **6**, 2100107.

6 W. Zhai, J. Zhu, Z. Wang, Y. Zhao, P. Zhan, S. Wang, G. Zheng, C. Shao, K. Dai, C. Liu and C. Shen, *ACS Appl. Mater. Interfaces*, 2022, **14**, 4562–4570.

7 Y. Zhao, M. Ren, Y. Shang, J. Li, S. Wang, W. Zhai, G. Zheng, K. Dai, C. Liu and C. Shen, *Compos. Sci. Technol.*, 2020, **200**, 108448.

8 S. Masihi, M. Panahi, D. Maddipatla, A. K. Bose, X. Zhang, A. J. Hanson, B. B. Narakathu, B. J. Bazuin and M. Z. Atashbar, *IEEE Sens. J.*, 2020, **20**, 7579–7587.

9 Z. Li, S. Chang, S. Khuje and S. Ren, *ACS Nano*, 2021, **15**, 6211–6232.

10 M. A. Seo, H. R. Park, S. M. Koo, D. J. Park, J. H. Kang, O. K. Suwal, S. S. Choi, P. C. M. Planken, G. S. Park, N. K. Park, Q. H. Park and D. S. Kim, *Nat. Photonics*, 2009, **3**, 152–156.

11 I. Llatser, C. Kremers, A. Cabellos-Aparicio, J. M. Jornet, E. Alarcón and D. N. Chigrin, *Photonics Nanostruct. – Fundam. Appl.*, 2012, **10**, 353–358.

12 M. Akbari, M. W. A. Khan, M. Hasani, T. Björninen, L. Sydänheimo and L. Ukkonen, *IEEE Antennas Wirel. Propag. Lett.*, 2016, **15**, 1569–1572.

13 G. S. Gund, M. G. Jung, K. Y. Shin and H. S. Park, *ACS Nano*, 2019, **13**, 14114–14121.

14 K. Zhu, C. Wen, A. A. Aljarb, F. Xue, X. Xu, V. Tung, X. Zhang, H. N. Alshareef and M. Lanza, *Nat. Electron.*, 2021, **4**, 775–785.

15 K. Y. Shin, J. Y. Hong and J. Jang, *Adv. Mater.*, 2011, **23**, 2113–2118.

16 X. Huang, T. Leng, X. Zhang, J. C. Chen, K. H. Chang, A. K. Geim, K. S. Novoselov and Z. Hu, *Appl. Phys. Lett.*, 2015, **106**, 203105.

17 M. Naguib, M. Kurtoglu, V. Presser, J. Lu, J. Niu, M. Heon, L. Hultman, Y. Gogotsi and M. W. Barsoum, *Adv. Mater.*, 2011, **23**, 4248–4253.

18 M. Naguib, O. Mashtalir, J. Carle, V. Presser, J. Lu, L. Hultman, Y. Gogotsi and M. W. Barsoum, *ACS Nano*, 2012, **6**, 1322–1331.

19 K. Hantanasirisakul and Y. Gogotsi, *Adv. Mater.*, 2018, **30**, 1804779.

20 M. Hu, H. Zhang, T. Hu, B. Fan, X. Wang and Z. Li, *Chem. Soc. Rev.*, 2020, **49**, 6666–6693.

21 Q. Jiang, N. Kurra, M. Alhabeb, Y. Gogotsi and H. N. Alshareef, *Adv. Energy Mater.*, 2018, **8**, 1703043.

22 M. Zhu, Y. Huang, Q. Deng, J. Zhou, Z. Pei, Q. Xue, Y. Huang, Z. Wang, H. Li, Q. Huang and C. Zhi, *Adv. Energy Mater.*, 2016, **6**, 1600969.

23 Y. Dall'Agnese, P. L. Taberna, Y. Gogotsi and P. Simon, *J. Phys. Chem. Lett.*, 2015, **6**, 2305–2309.

24 Q. Zhao, Q. Zhu, J. Miao, P. Zhang, P. Wan, L. He and B. Xu, *Small*, 2019, **15**, 1904293.

25 Y. Huang, Q. Lu, D. Wu, Y. Jiang, Z. Liu, B. Chen, M. Zhu and O. G. Schmidt, *Carbon Energy*, 2022, **4**, 598–620.

26 K. R. G. Lim, A. D. Handoko, S. K. Nemani, B. Wyatt, H. Y. Jiang, J. Tang, B. Anasori and Z. W. Seh, *ACS Nano*, 2020, **14**, 10834–10864.

27 Y. Pei, X. Zhang, Z. Hui, J. Zhou, X. Huang, G. Sun and W. Huang, *ACS Nano*, 2021, **15**, 3996–4017.

28 D. H. Ho, Y. Y. Choi, S. B. Jo, J. M. Myoung and J. H. Cho, *Adv. Mater.*, 2021, **33**, 2005846.

29 A. Sarycheva, T. Makaryan, K. Maleski, E. Satheeshkumar, A. Melikyan, H. Minassian, M. Yoshimura and Y. Gogotsi, *J. Phys. Chem. C*, 2017, **121**, 19983–19988.

30 L. Lan, X. Fan, S. Yu, J. Gao, C. Zhao, Q. Hao and T. Qiu, *ACS Appl. Mater. Interfaces*, 2022, **14**, 40427–40436.

31 K. Huang, Z. Li, J. Lin, G. Han and P. Huang, *Chem. Soc. Rev.*, 2018, **47**, 5109–5124.

32 B. Lyu, M. Kim, H. Jing, J. Kang, C. Qian, S. Lee and J. H. Cho, *ACS Nano*, 2019, **13**, 11392–11400.

33 X. Fu, L. Wang, L. Zhao, Z. Yuan, Y. Zhang, D. Wang, D. Wang, J. Li, D. Li, V. Shulga, G. Shen and W. Han, *Adv. Funct. Mater.*, 2021, **31**, 2010533.

34 C. Ma, M. G. Ma, C. Si, X.-X. Ji and P. Wan, *Adv. Funct. Mater.*, 2021, **31**, 2009524.

35 A. Ahmed, S. Sharma, B. Adak, M. M. Hossain, A. M. LaChance, S. Mukhopadhyay and L. Sun, *InfoMat*, 2022, **4**, e12295.

36 A. VahidMohammadi, J. Rosen and Y. Gogotsi, *Science*, 2021, **372**, eabf1581.

37 H. Kim, Z. Wang and H. N. Alshareef, *Nano Energy*, 2019, **60**, 179–197.

38 A. Sarycheva, A. Polemi, Y. Liu, K. Dandekar, B. Anasori and Y. Gogotsi, *Sci. Adv.*, 2018, **4**, eaau0920.

39 M. Han, Y. Liu, R. Rakhmanov, C. Israel, M. A. S. Tajin, G. Friedman, V. Volman, A. Hoorfar, K. R. Dandekar and Y. Gogotsi, *Adv. Mater.*, 2021, **33**, 2003225.

40 Y. Li, X. Tian, S. P. Gao, L. Jing, K. Li, H. Yang, F. Fu, J. Y. Lee, Y. X. Guo, J. S. Ho and P. Y. Chen, *Adv. Funct. Mater.*, 2020, **30**, 1907451.

41 Y. Shao, L. Wei, X. Wu, C. Jiang, Y. Yao, B. Peng, H. Chen, J. Huangfu, Y. Ying, C. J. Zhang and J. Ping, *Nat. Commun.*, 2022, **13**, 3223.

42 B. Anasori, M. R. Lukatskaya and Y. Gogotsi, *Nat. Rev. Mater.*, 2017, **2**, 16098.

43 M. Naguib, V. N. Mochalin, M. W. Barsoum and Y. Gogotsi, *Adv. Mater.*, 2014, **26**, 992–1005.

44 M. Ghidiu, M. R. Lukatskaya, M. Q. Zhao, Y. Gogotsi and M. W. Barsoum, *Nature*, 2014, **516**, 78–81.

45 O. Mashtalir, M. Naguib, V. N. Mochalin, Y. Dall'Agnese, M. Heon, M. W. Barsoum and Y. Gogotsi, *Nat. Commun.*, 2013, **4**, 1716.

46 O. Mashtalir, M. R. Lukatskaya, M. Q. Zhao, M. W. Barsoum and Y. Gogotsi, *Adv. Mater.*, 2015, **27**, 3501–3506.

47 M. Naguib, R. R. Unocic, B. L. Armstrong and J. Nanda, *Dalton Trans.*, 2015, **44**, 9353–9358.

48 R. Li, X. Ma, J. Li, J. Cao, H. Gao, T. Li, X. Zhang, L. Wang, Q. Zhang, G. Wang, C. Hou, Y. Li, T. Palacios, Y. Lin, H. Wang and X. Ling, *Nat. Commun.*, 2021, **12**, 1587.

49 K. Maleski, C. E. Shuck, A. T. Fafarman and Y. Gogotsi, *Adv. Opt. Mater.*, 2021, **9**, 2001563.

50 J. C. Lei, X. Zhang and Z. Zhou, *Front. Phys.*, 2015, **10**, 276–286.

51 X. Zhan, C. Si, J. Zhou and Z. Sun, *Nanoscale Horiz.*, 2020, **5**, 235–258.

52 K. Li, M. Liang, H. Wang, X. Wang, Y. Huang, J. Coelho, S. Pinilla, Y. Zhang, F. Qi, V. Nicolosi and Y. Xu, *Adv. Funct. Mater.*, 2020, **30**, 2000842.

53 H. E. Karahan, K. Goh, C. (John) Zhang, E. Yang, C. Yıldırım, C. Y. Chuah, M. G. Ahunbay, J. Lee, Ş. B. Tantekin-Ersolmaz, Y. Chen and T.-H. Bae, *Adv. Mater.*, 2020, **32**, 1906697.

54 W. Huang, L. Hu, Y. Tang, Z. Xie and H. Zhang, *Adv. Funct. Mater.*, 2020, **30**, 2005223.

55 M. R. Lukatskaya, S. Kota, Z. Lin, M. Q. Zhao, N. Shpigel, M. D. Levi, J. Halim, P. L. Taberna, M. W. Barsoum, P. Simon and Y. Gogotsi, *Nat. Energy*, 2017, **2**, 17105.

56 L. Qin, J. Jiang, Q. Tao, C. Wang, I. Persson, M. Fahlman, P. O. Å. Persson, L. Hou, J. Rosen and F. Zhang, *J. Mater. Chem. A*, 2020, **8**, 5467–5475.

57 J. Zhang, N. Kong, S. Uzun, A. Levitt, S. Seyedin, P. A. Lynch, S. Qin, M. Han, W. Yang, J. Liu, X. Wang, Y. Gogotsi and J. M. Razal, *Adv. Mater.*, 2020, **32**, 2001093.

58 P. Collini, S. Kota, A. D. Dillon, M. W. Barsoum and A. T. Fafarman, *J. Electrochem. Soc.*, 2017, **164**, D573.

59 Y. Y. Peng, B. Akuzum, N. Kurra, M. Q. Zhao, M. Alhabeb, B. Anasori, E. C. Kumbur, H. N. Alshareef, M. D. Ger and Y. Gogotsi, *Energy Environ. Sci.*, 2016, **9**, 2847–2854.

60 K. Khorsand Kazemi, E. Hosseini, S. Hu, R. Narang, S. Li, M. Arjmand and M. H. Zarifi, *Appl. Mater. Today*, 2022, **26**, 101294.

61 K. Li, Z. Li, Z. Xiong, Y. Wang, H. Yang, W. Xu, L. Jing, M. Ding, J. Zhu, J. S. Ho and P. Y. Chen, *Adv. Funct. Mater.*, 2022, **32**, 2110534.

62 K. Khorsand Kazemi, S. Hu, O. Niksan, K. K. Adhikari, N. R. Tanguy, S. Li, M. Arjmand and M. H. Zarifi, *Adv. Mater. Interfaces*, 2022, **9**, 2102411.